



Identification of Active Gold Nanoclusters on Iron Oxide Supports for CO Oxidation

Andrew A. Herzing, *et al.*
Science **321**, 1331 (2008);
DOI: 10.1126/science.1159639

This copy is for your personal, non-commercial use only.

If you wish to distribute this article to others, you can order high-quality copies for your colleagues, clients, or customers by [clicking here](#).

Permission to republish or repurpose articles or portions of articles can be obtained by following the guidelines [here](#).

The following resources related to this article are available online at www.sciencemag.org (this information is current as of December 9, 2010):

Updated information and services, including high-resolution figures, can be found in the online version of this article at:

<http://www.sciencemag.org/content/321/5894/1331.full.html>

Supporting Online Material can be found at:

<http://www.sciencemag.org/content/suppl/2008/09/04/321.5894.1331.DC1.html>

This article **cites 1 articles**, 1 of which can be accessed free:

<http://www.sciencemag.org/content/321/5894/1331.full.html#ref-list-1>

This article has been **cited by** 102 article(s) on the ISI Web of Science

This article has been **cited by** 4 articles hosted by HighWire Press; see:

<http://www.sciencemag.org/content/321/5894/1331.full.html#related-urls>

This article appears in the following **subject collections**:

Chemistry

<http://www.sciencemag.org/cgi/collection/chemistry>

17. J. Baker *et al.*, *Chem. Phys.* **178**, 569 (1993).
 18. A. Mellinger, C. R. Vidal, *J. Chem. Phys.* **101**, 104 (1994).
 19. J. Baker, F. Launay, *Chem. Phys. Lett.* **415**, 296 (2005).
 20. J. D. Simmons, S. G. Tilford, *J. Mol. Spectrosc.* **49**, 167 (1974).
 21. J. Baker, F. Launay, *J. Mol. Spectrosc.* **165**, 75 (1994).
 22. P. Cacciani, W. Hogervorst, W. Ubachs, *J. Chem. Phys.* **102**, 8308 (1995).
 23. P. Cacciani *et al.*, *Astrophys. J.* **499**, L223 (1998).
 24. G. Lim, S. M. Lim, S. K. Kim, Y. S. Choi, *J. Chem. Phys.* **111**, 456 (1999).
 25. S. K. Bhattacharya, J. Savarino, M. H. Thiemens, *Geophys. Res. Lett.* **27**, 1459 (2000).
 26. B. R. Lewis, S. T. Gibson, J. P. England, G. Stark, J. B. West, *J. Chem. Phys.* **116**, 3286 (2002).
 27. A. Pandey, S. K. Bhattacharya, *J. Chem. Phys.* **124**, 234301 (2006).
 28. M. L. Turnidge, J. P. Reid, P. W. Barnes, C. J. S. M. Simpson, *J. Chem. Phys.* **108**, 485 (1998).
 29. E. Anders, N. Grevesse, *Geochem. Cosmochim. Acta* **53**, 197 (1989).
 30. B. Fegley Jr., *Space Sci. Rev.* **92**, 177 (2000).
 31. E. D. Young, *Philos. Trans. R. Soc. Lond. A* **359**, 2095 (2001).
 32. E. D. Young, *Earth Planet. Sci. Lett.* **262**, 468 (2007).
 33. N. Sakamoto *et al.*, *Science* **317**, 231 (2007).
 34. Y. Yu, R. H. Hewins, R. N. Clayton, T. K. Mayeda, *Geochem. Cosmochim. Acta* **59**, 2095 (1995).
 35. This work was supported by NASA grant NNX07AJ81G under Origins and by the director, Office of Energy

Research, Office of Basic Energy Sciences, Chemical Sciences Division of the U.S. Department of Energy under contract DE-AC02-05CH11231. Three reviewers are thanked for helpful suggestions that improved the manuscript.

Supporting Online Material

www.sciencemag.org/cgi/content/full/321/5894/1328/DC1
 Methods
 Figs. S1 and S2
 Table S1
 References

15 April 2008; accepted 11 July 2008
 10.1126/science.1159178

Identification of Active Gold Nanoclusters on Iron Oxide Supports for CO Oxidation

Andrew A. Herzing,^{1,2} Christopher J. Kiely,^{1*} Albert F. Carley,³
 Philip Landon,³ Graham J. Hutchings^{3*}

Gold nanocrystals absorbed on metal oxides have exceptional properties in oxidation catalysis, including the oxidation of carbon monoxide at ambient temperatures, but the identification of the active catalytic gold species among the many present on real catalysts is challenging. We have used aberration-corrected scanning transmission electron microscopy to analyze several iron oxide-supported catalyst samples, ranging from those with little or no activity to others with high activities. High catalytic activity for carbon monoxide oxidation is correlated with the presence of bilayer clusters that are ~0.5 nanometer in diameter and contain only ~10 gold atoms. The activity of these bilayer clusters is consistent with that demonstrated previously with the use of model catalyst systems.

Gold nanoparticles on oxide supports are being used to catalyze an increasing number of reactions (1–6), but there is continuing interest in the relatively simple low-temperature oxidation of CO (1–3, 7), especially concerning the nature of the active species. Some proposals emphasize the size and morphology of the gold particle and its interface with the support (1, 8), whereas others postulate that the metal oxidation state (9, 10) and support material can have strong effects (1, 11). Most of the fundamental insights into this reaction have come from well-defined model studies (12–15) in which specific structures are tailor-made (14). However, the difficulty lies in linking these informative model studies to those carried out on real catalysts, which are inherently more complex. Here, we report a microscopy study of an Au/FeO_x catalyst and demonstrate that, among a number of gold nanostructures present, the origin of the activity is associated uniquely with gold bilayer nano-

clusters that are ~0.5 nm in diameter and contain ~10 Au atoms.

Gold supported on FeOOH is a highly active catalyst for the low-temperature oxidation of CO (16), and we recently reported a link between catalyst performance and catalyst drying conditions (10). A pair of 2.9 atomic % Au/FeO_x samples (denoted samples 1 and 2) were derived from the same coprecipitated precursor. Sample 1 was dried in a tube furnace (static air; furnace was ramped after insertion at 15°C/min to 120°C; 16 hours), whereas sample 2 was dried in a gas chromatog-

raphy (GC) oven (flowing air; sample inserted into the furnace at 120°C; 16 hours). The Au loading in each was identical, and the underlying disordered FeOOH supports had similar surface areas (~190 m² g⁻¹). X-ray energy-dispersive spectroscopy (XEDS) analysis and high-angle annular dark-field (HAADF) imaging experiments (10) indicated that both samples contained 2- to 15-nm Au particles, with mean particle sizes of 5.4 nm for sample 1 and 7.0 nm for sample 2.

If the CO oxidation activity was dictated solely by the Au particle size, as some researchers have suggested (1, 8), then these two samples should have exhibited similar activities. In fact, sample 1 would probably be expected to have a slightly better performance by virtue of the Au particles being slightly smaller, on average. However, catalytic testing of these two samples under standard conditions (total flow rate of 66,000 h⁻¹; 0.5 volume % CO) revealed that sample 2 achieved 100% CO conversion at 25°C, whereas sample 1 gave only trace CO conversion (<1%). Even at much higher flow rates, sample 2 remained active (i.e., at a total flow rate of 450,000 vol.gas/vol.catalyst.h; the conversion was 25%), whereas sample 1 was totally inactive. Previously (10), we were unable to determine the origin of this marked effect because of the resolution and sensitivity limitations of the characterization techniques available. We consider that at least two possibilities exist to explain this difference: (i) There could be highly dispersed Au species present in sample 2 that were beyond the resolution limit of the conventional HAADF and

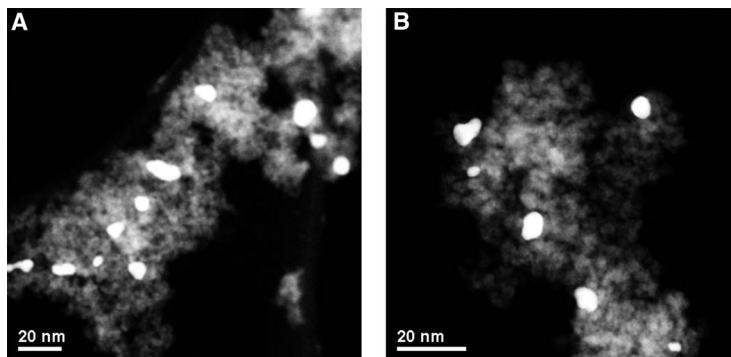


Fig. 1. Low-magnification aberration-corrected HAADF-STEM images from (A) the inactive, tube furnace catalyst (sample 1) and (B) the highly active, GC oven catalyst (sample 2). Au particle size distribution in both samples appears to be very similar at this magnification.

¹Center for Advanced Materials and Nanotechnology, Lehigh University, 5 East Packer Avenue, Bethlehem, PA 18015–3195, USA. ²National Institute of Standards and Technology, Surface and Microanalysis Science Division, 100 Bureau Drive, Mailstop 8371, Gaithersburg, MD 20899–8371, USA. ³Cardiff Catalysis Institute School of Chemistry, Cardiff University, Cardiff, CF10 3AT, UK.

*To whom correspondence should be addressed. E-mail: chk5@lehigh.edu (C.J.K.); hutch@cardiff.ac.uk (G.J.H.)

scanning transmission electron microscopy (STEM)–XEDS techniques used previously, or (ii) the active catalyst contained some form of cationic Au species that was absent in the inactive sample. These two possibilities need not be mutually exclusive.

To investigate this unexpected difference in reactivity, we re-examined the samples using a state-of-the-art JEOL 2200FS in STEM mode equipped with a double-hexapole spherical aberration corrector manufactured by CEOS GmbH (17). The improvement to the HAADF image resolution, from the use of a 0.1-nm diameter aberration-corrected STEM probe containing 50 pA of current, makes this an ideal instrument to test whether there were Au species present in the highly active sample that were not detected earlier (10). Previously, this method has successfully been used to image atomic dispersions in the La/Al₂O₃, Pt/Al₂O₃, and Au/TiO₂ systems (18). The lower-magnification HAADF images for each of the dried Au/FeO_x catalysts (Fig. 1, A and B) confirm the earlier results, with particles between 2 and 15 nm in diameter. However, at higher magnification (Fig. 2, A to D, and figs. S1 and S2), the actual Au particle size distribution and morphology in these samples are quite different. Both samples contain larger (2 to 15 nm) Au particles and a considerable number of individual Au atoms (indicated by white circles) dispersed on the iron oxide surface.

The observation of these individual atoms ensures that we are now resolving all of the types of Au species present. However, in addition a large population of subnanometer Au clusters was found in the active sample 2 (circled in black in Fig. 2, C and D) (see also fig. S1) that was not detected in the inactive sample. These Au clusters, the majority of which were 0.2 to 0.5 nm in diameter, contain at most only a few Au atoms. The contrast level exhibited by the 0.2- to 0.3-nm clusters, which are predominant in Fig. 2D, is similar to that of the individual Au atoms, implying that they are monolayer structures. In comparison, the 0.5-nm clusters highlighted in Fig. 2C exhibit markedly higher contrast in the HAADF image than that of the 0.2- to 0.3-nm clusters, suggesting that these larger clusters are most likely bilayers of Au.

Determination of the exact number of atoms in these various structures is complicated by several factors, including the slight contraction of the Au–Au bond distance known to occur in particles of this size (19). However, a rough estimate is still informative, and bilayers of ~0.5-nm lateral dimension would contain ~10 atoms (fig. S3A). In comparison, the 0.2- to 0.3-nm clusters of similar contrast to monolayers could contain about three to four atoms (fig. S3B). In contrast, an estimate based on the volumetric packing density of Au (~59 atoms/nm³) suggests that the larger nanoparticles (5 to 7 nm) would contain 1900 to 5250 atoms if they have a hemispherical geometry. Thus, the subnanometer clusters and individual atoms observed in the highly active sample represent only a very minor fraction of the total Au content.

We used atomic-resolution STEM imaging to estimate the number fraction of the total Au particles represented by both clusters and nanoparticles by surveying several support areas that had ~100 larger nanoparticles, along with their neighboring vicinities (17). In terms of their frequency of observation, the individually adsorbed Au atoms represented 44 ± 4.5% of the Au species, whereas 19 ± 3.4% were 0.2- to 0.3-nm clusters, 18 ± 3.0% were 0.3- to 0.5-nm clusters, and 19 ± 3.5% were particles >1 nm (~50% were >5 nm).

However, considering the number of Au atoms in each of these structures (as discussed above) suggests that the individual atoms represent only 0.13 ± 0.07 atomic % and that the monolayer and bilayer subnanometer clusters combined represent only 1.05 ± 0.72 atomic % of the total Au loading (18), with the remaining 98.82 ± 0.80 atomic % of Au contained in the larger particles. Because of the very large disparity in the number of atoms they contain, the number of subnanometer clusters would have to exceed that of the 5-nm particles by a margin of nearly four to one for them to represent just 2 atomic % of the total Au loading. Therefore, it is probable that these minority Au species would not be easily detected with traditional “bulk” techniques such as extended x-ray absorption fine structure or Mossbauer spectroscopy, or even by surface analysis techniques such as x-ray photo-

electron spectroscopy (XPS), because their contribution to the total signal would be minimal compared with that of the larger nanoparticles (17).

The statistical accuracy of the current HAADF analysis must be considered, because undercounting of the subnanometer Au clusters may result from the nature of the STEM imaging process in an aberration-corrected instrument. The ability to detect single atoms on an oxide is highly dependent on the vertical position of the focused electron probe relative to the surface (20). Because adsorbed atoms can be present on either the top or bottom surface of the underlying oxide particle, imaging with single-atom resolution is possible only when one of the surfaces is exactly in focus. Practically, this limitation means that in any given image, single atoms are probably only detected on one surface of the support particle, and atoms on the opposite side may not be visible, whereas larger nanoparticles can be detected on either side of the support over a much wider range of defocus values. In the intermediate case of 0.2- to 0.5-nm clusters, it is not clear if the same narrow defocus range required to resolve individual atoms is necessary. However, even if it is pessimistically assumed that our analysis has detected only 50% of the total number of all the individual Au atoms, the atomically dispersed Au would still represent only 61 ± 3.6% of the total number of

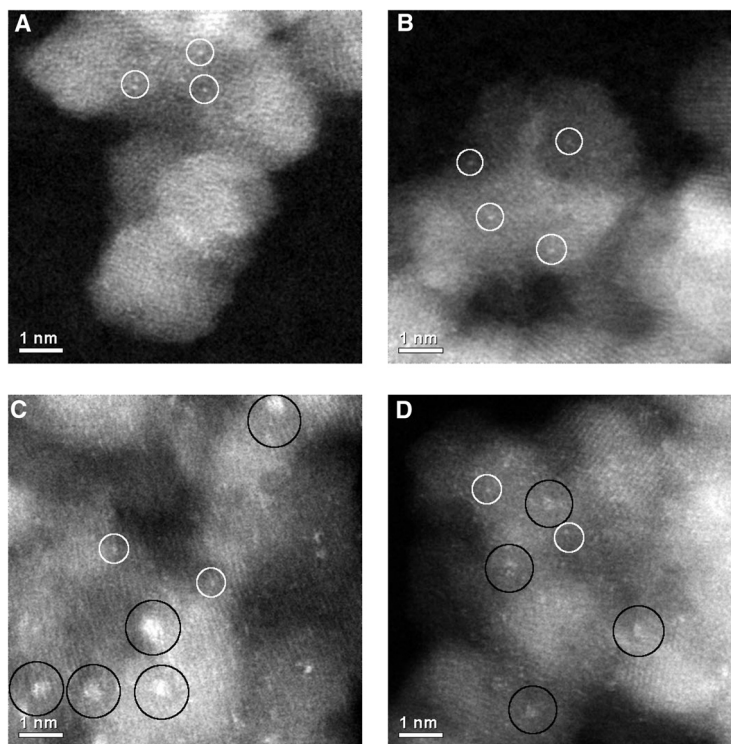


Fig. 2. High-magnification aberration-corrected STEM-HAADF images of (A and B) the inactive (sample 1) and (C and D) the active (sample 2) Au/FeO_x catalysts acquired with the aberration-corrected JEOL 2200FS. The white circles indicate the presence of individual Au atoms, whereas the black circles indicate subnanometer Au clusters consisting of only a few atoms. Note the presence and image intensity difference of two distinct cluster-types: In (C) there are 0.5 nm higher-contrast clusters, whereas in (D) 0.2- to 0.3-nm low-contrast clusters dominate. This difference indicates that bilayer and monolayer subnanometer Au clusters are present in the active catalyst.

Au species, or $\sim 0.25 \pm 0.2$ atomic % of the total Au loading.

The observation that the active species in our Au/FeO_x catalysts consist of subnanometer clusters differs from numerous earlier investigations that identified 2- to 5-nm particles as the critical “nanostructure.” However, a number of recent experimental and theoretical (21–23) studies have suggested that the CO oxidation activity should continue to increase as the Au particle size approaches 1 nm because of the presence of a larger fraction of Au atoms with low coordination in the smaller particles. Low-coordination Au atoms possess a d-band that is closer to the Fermi level than their close-packed counterparts, so they can adsorb O₂ molecules more readily. More specifically, Falsig *et al.* predicted that adsorption energies for CO and O are ideally suited for maximizing the reaction rate of CO oxidation at sixfold coordinated Au corner atoms, whereas the adsorption energies at close-packed Au faces are inferior for this purpose (23). Because clusters smaller than 1 nm should have an even greater fraction of low-coordinated Au atoms, reaching $\sim 90\%$ as a cluster size of 0.5 nm is approached, the role of subnanometer clusters may be crucial. Rashkeev *et al.* (24) have recently presented HAADF evidence that subnanometer mono-, bi-, and trilayer Au clusters coexisted in active Au/TiO₂ catalysts, although they were unable to isolate the relative importance of each of these subnanometer species and did not report any spectroscopic measurements to determine the possible role of substrate surface chemistry.

Scanning tunneling microscopy studies on model catalysts by Matthey *et al.* (15) showed that subtle changes in the chemistry of an oxide surface could alter the energetically favorable Au

structures that it stabilized and supported. Specifically, an oxygen-rich TiO₂ (110) surface could stabilize a range of Au species from one to seven atoms in size. In contrast, single Au atoms and Au trimers were the only stable configurations on a reduced TiO₂ (110) surface, whereas weakly bonded two-dimensional Au raftlike species were the only stable structures on a stoichiometric TiO₂ (110) surface. Similar oxygen-rich surfaces to those reported for TiO₂ have also been identified for FeO_x (25); however, to our knowledge, systematic surface science studies and first-principle calculations of the stable Au structures present on FeOOH or Fe₂O₃ have not yet been performed.

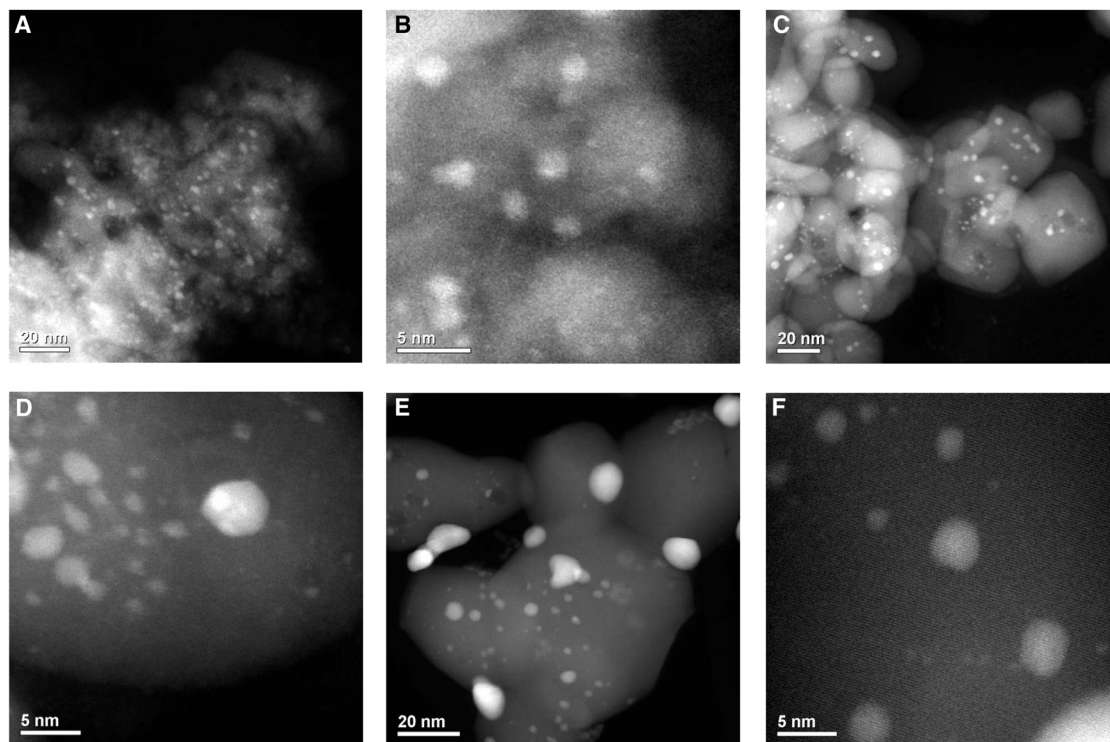
On the basis of the observations of the two dried catalysts alone, we are unable to definitively comment on whether the bilayer 0.5-nm clusters, the monolayer 0.2- to 0.3-nm clusters, or both are responsible for the high activity observed or whether some subtle substrate chemistry effect is coming into play. Although individual Au atoms and larger (3 to 5 nm) particles are stable on both catalysts, the subnanometer Au clusters were only stable on the surface of catalyst 2 dried under a flowing air. The critical role played by such slight changes in the catalyst preparation route may help to explain the sometimes radically differing activities reported. We have used XPS to probe the nature of the surface species present in both samples. Analysis of the Au(4f) spectra (fig. S4.1) showed that, in both catalysts, the Au(4f_{7/2}) binding energy was 85.1 eV, characteristic of Au⁺ species. The signal from sample 1 shows some broadening to higher binding energy that probably arose from a small amount of Au³⁺, most likely present as AuOOH. The presence of hydroxylated Au species in this inactive sample suggests that the

lack of air circulation during the drying process inhibits the removal of the hydroxyl species from the catalyst surface, whereas this process occurs more efficiently under flowing air conditions.

This explanation was confirmed by the O(1s) and C(1s) spectra from these samples (figs. S4.2 and S4.3, respectively). Both catalysts exhibit a main O(1s) component characteristic of oxidic oxygen (O²⁻) at 530.4 eV, together with a shoulder at 531.8 eV. The latter feature originates from a combination of hydroxyl and carbonate species and is much more pronounced in sample 1. The C(1s) spectra, which show clear evidence of carbonate species, are similar for both. Therefore, the higher intensity of the O(1s) shoulder at 531.8 eV in the inactive catalyst 1 arises from the increased presence of hydroxyl groups relative to the active catalyst 2 dried in flowing air. This higher degree of hydroxylation and reduction of sample 1 seems to enhance the ability of the subnanometer clusters to sinter into larger particles and thus deactivate the catalyst. Hence, on the basis of the evidence presented so far, we are unable to determine whether it is the presence of subnanometer clusters or the differing degree of hydroxylation of the support that is controlling the activity.

Three separate portions of the highly active catalyst 2, denoted 3, 4, and 5, were calcined (3 hours at 400°, 550°, and 600°C, respectively). These heat treatments converted the support material to crystalline Fe₂O₃ and progressively reduced the surface area (catalysts 2: 190 m² g⁻¹, 3: 45 m² g⁻¹, 4: 16 m² g⁻¹, and 5: 11 m² g⁻¹). Atomic absorption spectroscopy confirmed that all of the Au (2.9 atomic %) was retained. CO conversion decreased from 100% in the fresh, uncalcined state to 91% (400°C), 31% (550°C), and <1% (600°C).

Fig. 3. Aberration-corrected STEM-HAADF images of the active 2.9 atomic % Au/FeO_x catalyst 2 calcined for 3 hours at (A and B) 400°C (sample 3), (C and D) 550°C (sample 4), and (E and F) 600°C (sample 5). The heat-treatment procedures have substantially decreased the population of subnanometer Au clusters relative to the highly active, dried catalyst, while at the same time they have increased the population of particles in the 1- to 3-nm range.



Aberration-corrected STEM-HAADF images (Fig. 3, A to F, and figs. S5.1 to 5.3) revealed that, although substantial particle sintering had occurred in all calcined catalysts, each sample also retained a population of the subnanometer clusters and individual Au atoms previously seen in the dried catalyst that had persisted through the various calcination treatments.

The number frequency of the various gold species encountered in samples 2, 3, 4, and 5 is summarized in Fig. 4. The number fraction of atomically dispersed species drops from ~44% to 35% across this sample set, whereas, simultaneously, the number fraction of particles greater than 1 nm progressively increases from 19 to 35%. However, our previous deductions from comparing samples 1 and 2 indicate that the supported subnanometer cluster species (and not the dispersed Au atoms or >1-nm particles) are active for CO conversion. It is also apparent from Fig. 4 that the number population of monolayer clusters remains relatively

constant at ~19%, whereas the bilayer cluster frequency gradually drops from 18% to <5% across this same sample set. Hence, the dramatic decrease in catalytic activity exhibited by samples 3, 4 and 5 can be directly correlated to the marked decrease in the number density of the 0.5-nm bilayer clusters as a result of their sintering into less active 1- to 2-nm Au particles.

XPS of samples 3, 4, and 5 (fig. S6) showed no notable difference in either of the Au(4f), Fe(3s), or Fe(2p) profiles (fig. S6.1 and 6.2) associated with this series of calcined catalysts. The O(1s) signals (fig. S6.3) are also all similar, with a high-binding energy tail indicating the presence of some residual hydroxyl and carbonate species, but these are very different from the dried sample (spectra shown in Fig. 5). The presence of carbonate species is confirmed by the weak, high binding feature in the C(1s) spectra (fig. S6.4). This feature is broader for sample 5, possibly reflecting carbonate species in distinct chemical envi-

ronments, and is consistent with small differences in the high-binding energy tail in the O(1s) spectrum for this sample.

To determine whether the small differences in samples 3 and 4 and the larger differences with the other samples correlate with the catalytic performance, we deconvoluted the O 1s signals into oxide and the higher-binding energy hydroxyl and carbonate species to obtain the relative fractions of each species present. However, the data for either the relative area percent of the higher-binding energy species (samples 2: 60%, 3: 28%, 4: 34%, and 5: 47%) or the hydroxyl/oxide ratio (samples 2: 1.5, 3: 0.4, 4: 0.5, and 5: 0.9) do not correlate with the observed activity trend. Thus, the similarity in the surface chemistry of samples 3 and 4, in particular, and the Au oxidation state in these calcined samples strongly imply that the progressive decrease in catalytic activity upon sintering is attributable to the gradual decrease in the population of the subnanometer bilayer clusters of gold.

Theoretical and model studies (23, 26–29) have shown that a critical factor in the catalytic activity of Au is the ability of the clusters to simultaneously adsorb both reactant molecules. Yoon *et al.* and Hakkinen *et al.* (27, 28) showed that the smallest Au cluster on MgO known to be active for CO oxidation is an octamer. Our observations are consistent with these theoretical studies, because the active bilayer subnanometer clusters in our system contain ~10 atoms, whereas the monolayer clusters (which have only three to four atoms) and the isolated Au atoms appear to be essentially inactive for CO oxidation.

Finally, CO oxidation activity of model Au catalysts on TiO₂ surfaces is maximized when the Au structures are two atomic layers thick (14, 28, 29), resulting in turnover frequencies (TOFs) as high as 3.7 s⁻¹. In the present case, the TOF of catalyst 2 exhibiting 100% CO conversion was initially calculated to be 0.016 s⁻¹ under standard conditions and 0.027 s⁻¹ at the higher flow rate where total conversion (which is a more reliable estimate of the catalyst activity) was not observed. However, if the TOF is recalculated assuming that the bilayer clusters are the only active species and using a reasonable estimate of the fraction of the total Au that they contain (0.6 atomic %), the result is a TOF of 2.7 s⁻¹ at the standard conditions and 3.5 s⁻¹ at the higher-flow rate condition. These re-estimated TOF values are reasonably similar to the value of 3.7 s⁻¹ of the model Au/TiO₂ catalyst (14).

These studies describe the full range of active and inactive Au species that are present within supported Au/FeO_x and Au/Fe₂O₃ catalysts. Subtle changes in sample-preparation route and calcination temperature can influence the formation, stability, and relative population of these various Au species. Herein, we have reported that highly active subnanometer Au clusters can be synthesized with a traditional chemical preparation route. Although the highest-activity catalysts correspond to uncalcined materials, experiments involving systematic calcination treatments have allowed us to

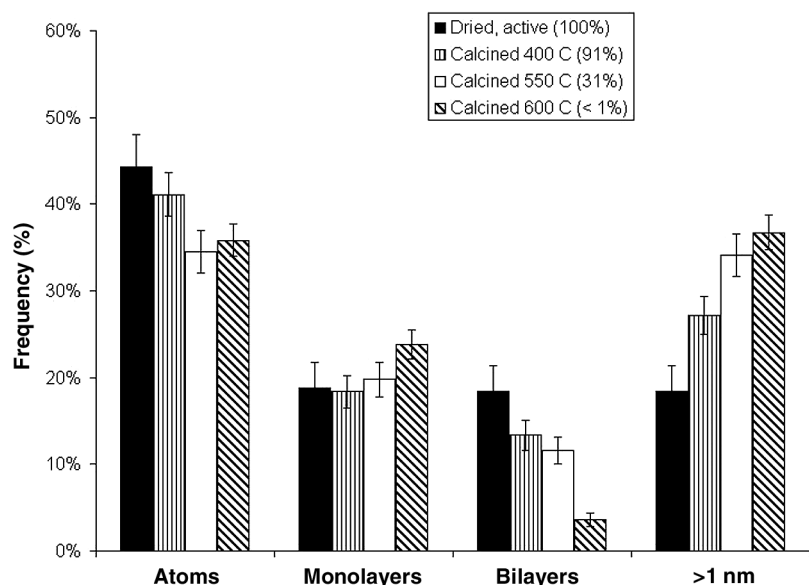
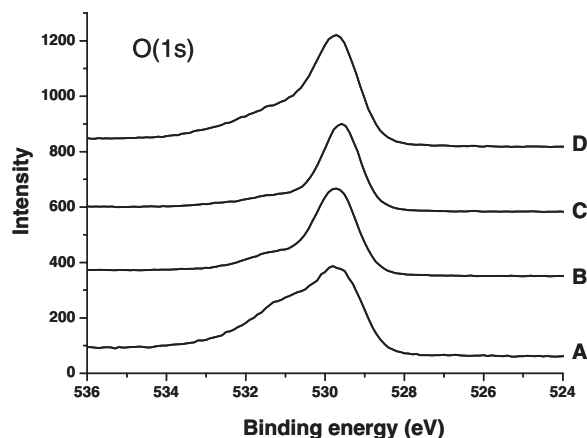


Fig. 4. Relative populations of (i) dispersed Au atoms, (ii) 0.2- to 0.3-nm monolayer Au clusters, (iii) 0.5-nm bilayer Au clusters, and (iv) Au nanoparticles >1 nm in diameter, as a function of catalyst calcination temperature and measured CO conversion. The error bars correspond to two SDs on the size measurements.

Fig. 5. O(1s) photoemission spectra from the Au/Fe₂O₃ catalysts (A) dried at 120°C and then calcined at (B) 400°C, (C) 550°C, and (D) 600°C.



deduce that it is primarily the 0.5-nm bilayer clusters, rather than 0.2- to 0.3-nm monolayer Au clusters, that are active for CO oxidation on FeO_x supports.

References and Notes

1. M. Haruta, *CATTECH* **6**, 102 (2002).
2. M. Haruta, *Gold Bull.* **37**, 27 (2004).
3. A. S. K. Hashmi, G. J. Hutchings, *Angew. Chem. Int. Ed.* **45**, 7896 (2006).
4. M. D. Hughes *et al.*, *Nature* **437**, 1132 (2005).
5. D. I. Enache *et al.*, *Science* **311**, 362 (2006).
6. A. Corma, P. Serna, *Science* **313**, 332 (2006).
7. J. Guzman, S. Carrettin, A. Corma, *J. Am. Chem. Soc.* **127**, 3286 (2005).
8. J. J. Pietron, R. M. Stroud, D. R. Rolison, *Nano Lett.* **2**, 545 (2002).
9. J. Guzman, B. C. Gates, *J. Am. Chem. Soc.* **126**, 2672 (2004).
10. G. J. Hutchings *et al.*, *J. Catal.* **242**, 71 (2006).
11. M. M. Schubert *et al.*, *J. Catal.* **197**, 113 (2001).
12. R. Meyer, C. Lemire, Sh. K. Shaikhutdinov, H.-J. Freund, *Gold Bull.* **37**, 72 (2004).
13. M. Valden, X. Lai, D. W. Goodman, *Science* **281**, 1647 (1998).
14. M. S. Chen, D. W. Goodman, *Science* **306**, 252 (2004), published online 26 August 2004; 10.1126/science.1102420.
15. D. Matthey *et al.*, *Science* **315**, 1692 (2007).
16. N. A. Hodge *et al.*, *Catal. Today* **72**, 133 (2002).
17. Materials and methods are available as supporting material on Science Online.
18. M. Varela *et al.*, *Annu. Rev. Mater. Res.* **35**, 539 (2005).
19. C. W. Mays *et al.*, *Surf. Sci.* **12**, 134 (1968).
20. S. Wang *et al.*, *Nat. Mater.* **3**, 143 (2004).
21. T. V. W. Janssens *et al.*, *Top. Catal.* **44**, 15 (2007).
22. W. Yan *et al.*, *J. Phys. Chem. B* **109**, 10676 (2005).
23. H. Falsig *et al.*, *Angew. Chem. Int. Ed.* **47**, 4835 (2008).
24. S. Rashkeev *et al.*, *Phys. Rev. B* **76**, 035438 (2007).
25. A. Bongiorno, U. Landman, *Phys. Rev. Lett.* **95**, 106102 (2005).
26. M. Abu Haija *et al.*, *Surf. Sci.* **600**, 1497 (2006).
27. B. Yoon *et al.*, *Science* **307**, 403 (2005).
28. H. Hakkinen *et al.*, *Angew. Chem. Int. Ed.* **42**, 1297 (2003).
29. V. A. Bondzie *et al.*, *Catal. Lett.* **63**, 143 (1999).
30. We thank the Athena project of the Engineering and Physical Sciences Research Council, NSF, NASA, and the National Research Council Postdoctoral Associate program for funding this work.

Supporting Online Material

www.sciencemag.org/cgi/content/full/321/5894/1331/DC1
Materials and Methods
Figs. S1 to S6
25 April 2008; accepted 23 July 2008
10.1126/science.1159639

Laser Frequency Combs for Astronomical Observations

Tilo Steinmetz,^{1,2} Tobias Wilken,¹ Constanza Araujo-Hauck,³ Ronald Holzwarth,^{1,2} Theodor W. Hänsch,¹ Luca Pasquini,³ Antonio Manescau,³ Sandro D'Odorico,³ Michael T. Murphy,⁴ Thomas Kentischer,⁵ Wolfgang Schmidt,⁵ Thomas Udem^{1*}

A direct measurement of the universe's expansion history could be made by observing in real time the evolution of the cosmological redshift of distant objects. However, this would require measurements of Doppler velocity drifts of ~ 1 centimeter per second per year, and astronomical spectrographs have not yet been calibrated to this tolerance. We demonstrated the first use of a laser frequency comb for wavelength calibration of an astronomical telescope. Even with a simple analysis, absolute calibration is achieved with an equivalent Doppler precision of ~ 9 meters per second at ~ 1.5 micrometers—beyond state-of-the-art accuracy. We show that tracking complex, time-varying systematic effects in the spectrograph and detector system is a particular advantage of laser frequency comb calibration. This technique promises an effective means for modeling and removal of such systematic effects to the accuracy required by future experiments to see direct evidence of the universe's putative acceleration.

Recent cosmological observations suggest that the universe's expansion is accelerating. Several lines of evidence corroborate this, including results from distant supernovae (1, 2), the cosmic microwave background (3), and the clustering of matter (4, 5). However, the current observations are all essentially geometric in nature, in that they map out space, its curvature, and its evolution. In contrast, a direct and dynamical determination of the universe's expansion history is possible by observing the slow drift of cosmological redshifts, z , that is inevitable in any evolving universe (6). No particular cosmological model or theory of gravity would be needed to interpret the results of such an experiment. However, the cosmological redshift drift is exceedingly small and

difficult to measure; for currently favored models of the universe, with a cosmological constant parametrizing the acceleration, the redshifts of objects drift by less than ~ 1 cm s⁻¹ year⁻¹ (depending on their redshifts).

Nevertheless, the suggestion that the so-called Lyman- α "forest" seen in high-redshift quasar spectra is the best target for this experiment (7) was recently supported by cosmological hydrodynamical simulations (8). The forest of absorption lines is caused by the Lyman- α transition arising in neutral hydrogen gas clouds at different redshifts along the quasar sight-lines. Detailed calculations with simulated quasar spectra show that the planned 42-m European Extremely Large Telescope (E-ELT), equipped with the proposed Cosmic Dynamics Experiment (CODEX) spectrograph (9), could detect the redshift drift convincingly with 4000 hours of observing time over a ~ 20 -year period (8). Therefore, as the observation is feasible (in principle), overcoming the many other practical challenges in such a measurement is imperative. Important astrophysical and technical requirements have been considered in detail, and most are not difficult to surmount (8, 10). One (but not the only) extremely important requirement is

that the astronomical spectrographs involved must have their wavelength scales calibrated accurately enough to record ~ 1 cm s⁻¹ velocity shifts (~ 25 -kHz frequency shifts) in the optical range. Moreover, this accuracy must be repeatable over ~ 20 -year time scales.

Although the redshift drift experiment requires demanding precision and repeatability, precisely calibrated astronomical spectrographs have several other important applications. For example, Jupiter- and Neptune-mass extrasolar planets have been discovered by the reflex Doppler motion of their host stars (11–13), but detecting Earth-mass planets around solar-mass stars will require ~ 5 cm s⁻¹ precision maintained over several-year time scales (14). Another example is the search for shifts in narrow quasar absorption lines caused by cosmological variations in the fundamental constants of nature (15–17). Recent measurements (18–21) achieve precisions of ~ 20 m s⁻¹, but the possibility of hidden systematic effects, and the increased photon-collecting power of future ELTs, warrant much more precise and accurate calibration over the widest possible wavelength range.

Laser frequency combs (LFCs) offer a solution because they provide an absolute, repeatable wavelength scale defined by a series of laser modes equally spaced across the spectrum. The train of femtosecond pulses from a mode-locked laser occurs at the pulse repetition rate, f_{rep} , governed by the adjustable laser cavity length. In the frequency domain, this yields a spectrum, $f_n = f_{\text{ceo}} + n \times f_{\text{rep}}$, with modes enumerated by an integer $n \sim 10^5$ to 10^6 . The carrier envelope offset frequency, $f_{\text{ceo}} \leq f_{\text{rep}}$, accounts for the laser's internal dispersion, which causes the group and phase velocities of the pulses to differ (22). Thanks to the large integer n , the optical frequencies f_n are at hundreds of THz whereas both f_{rep} and f_{ceo} are radio frequencies and can be handled with simple electronics and stabilized by an atomic clock (22). Each mode's absolute frequency is known to a precision limited only by the accuracy of the clock. Even low-cost, portable atomic clocks provide ~ 1 cm s⁻¹ (or 3 parts in 10^{11}) precision. Because LFC light power is much higher than required, the calibration precision possible is therefore limited by the maximum signal-to-noise

¹Max-Planck Institut für Quantenoptik, Hans-Kopfermann-Strasse 1, D-85748 Garching, Germany. ²Menlo Systems GmbH, Am Klopferpitz 19, D-82152 Martinsried, Germany. ³European Southern Observatory, Karl-Schwarzschild-Strasse 3, D-85748 Garching, Germany. ⁴Centre for Astrophysics and Supercomputing, Swinburne University of Technology, Mail H39, Post Office Box 218, Victoria 3122, Australia. ⁵Kiepenheuer-Institut für Sonnenphysik, Schöneckstr. 6, D-79104 Freiburg, Germany.

*To whom correspondence should be addressed. E-mail: thu@mpq.mpg.de